



Contents lists available at ScienceDirect

Journal of the European Ceramic Society

journal homepage: www.elsevier.com/locate/jeurceramsoc

MgAl₂O₄ spinel with transmittance approaching theoretical value at reduced sintering temperatures

Paulina Zubrzycka^{a,b,*}, Marta Radecka^b, Thomas Graule^a, Anita Trenczek-Zajac^b,
Dariusz Zientara^b, Michael Stuer^{a,**}

^a Laboratory for High Performance Ceramics, Empa, Überlandstrasse 129, Dübendorf 8600, Switzerland

^b Faculty of Materials Science and Ceramics, AGH University of Science and Technology, al. Adama Mickiewicza 30, Krakow 30-059, Poland

ARTICLE INFO

Keywords:

MgAl₂O₄

Spinel

Doping

Sintering

HIP

Transparent ceramics

ABSTRACT

Magnesium aluminate spinel is known to be a material with a good combination of mechanical properties, resistance against chemical attack and a high melting point, being thus a very promising material for application as a transparent material in harsh, high-temperature environments where glass fails. To improve the control over the microstructural evolution during sintering, Eu³⁺, Y³⁺ Mg²⁺ and their combinations were introduced as doping elements. The goal of the study was to optimize processing of fine spinel powder and investigate the potential for enhancing MgAl₂O₄ spinel density and in-line transmittance by using elements segregating to grain boundaries. The total and in-line transmittance were measured, and the characteristic pore size for transparent samples calculated based on the Rayleigh scattering approximation. Eu-doping proved to be effective in lowering the residual pore size and thus achieving in-line transmittance approaching the theoretical value at relatively low sintering temperatures (1400 °C).

1. Introduction

Transparent ceramics are of particular relevance for applications in high temperature technologies, infrared (IR) windows, optoelectronic components, transparent armors or lamp envelopes, among others. High transmittance can be achieved by reducing absorption and scattering cross sections to the lowest possible level [1–3]. The absorption processes are the result of electron transitions (in the high energy range, UV light), vibrational and rotational changes (in the lower energy range, IR), e.g., for amorphous materials, as well as point defects that contribute to absorption in various parts of the spectrum [4]. The scattering losses are caused by differences in the refractive indices that may be caused either by the presence of secondary phases, pores and inhomogeneities or the anisotropic nature of the material itself (e.g. non-cubic structure) leading to the appearance of birefringence [1,2,5]. It is however worth mentioning that at very high energies ($\lambda \approx 200$ nm), even MgAl₂O₄ with its cubic structure starts exhibiting birefringence [6].

Following the Lambert-Beer law, the real in-line transmittance (RIT) decreases exponentially with the sample thickness (d) and the total

scattering/absorption coefficient (γ_{tot}) (taking into account all absorption/scattering/reflection events), where R_s – reflection losses are equal to the maximum theoretical transmittance T_{max} :

$$RIT = (1 - R_s) \exp(-\gamma_{tot}d) \quad (1)$$

In the case of spinel in the absence of color centers and wavelength longer than 200 nm, the total scattering/absorption coefficient becomes the total scattering coefficient, which is the sum of the grain-boundary scattering coefficient (γ_{gb}), pores scattering coefficient (γ_{pores}):

$$\gamma_{tot} = \gamma_{gb} + \gamma_{pores} \quad (2)$$

Indeed, MgAl₂O₄ being a cubic isotropic material, the differences in the refractive index between two neighboring grains can be assumed negligible. Therefore, the total scattering coefficient can be reduced to the pores' scattering coefficient:

$$\gamma_{tot} = \gamma_{pores} \quad (3)$$

Accordingly, the transparency of spinel may be assumed to be only a function of porosity/density, omitting the need for stringent grain size control as in the case of transparent polycrystalline alumina, for

* Corresponding author at: Laboratory for High Performance Ceramics, Empa, Überlandstrasse 129, Dübendorf 8600, Switzerland.

** Corresponding author.

E-mail addresses: paulina.zubrzycka@agh.edu.pl (P. Zubrzycka), michael.stuer@empa.ch (M. Stuer).

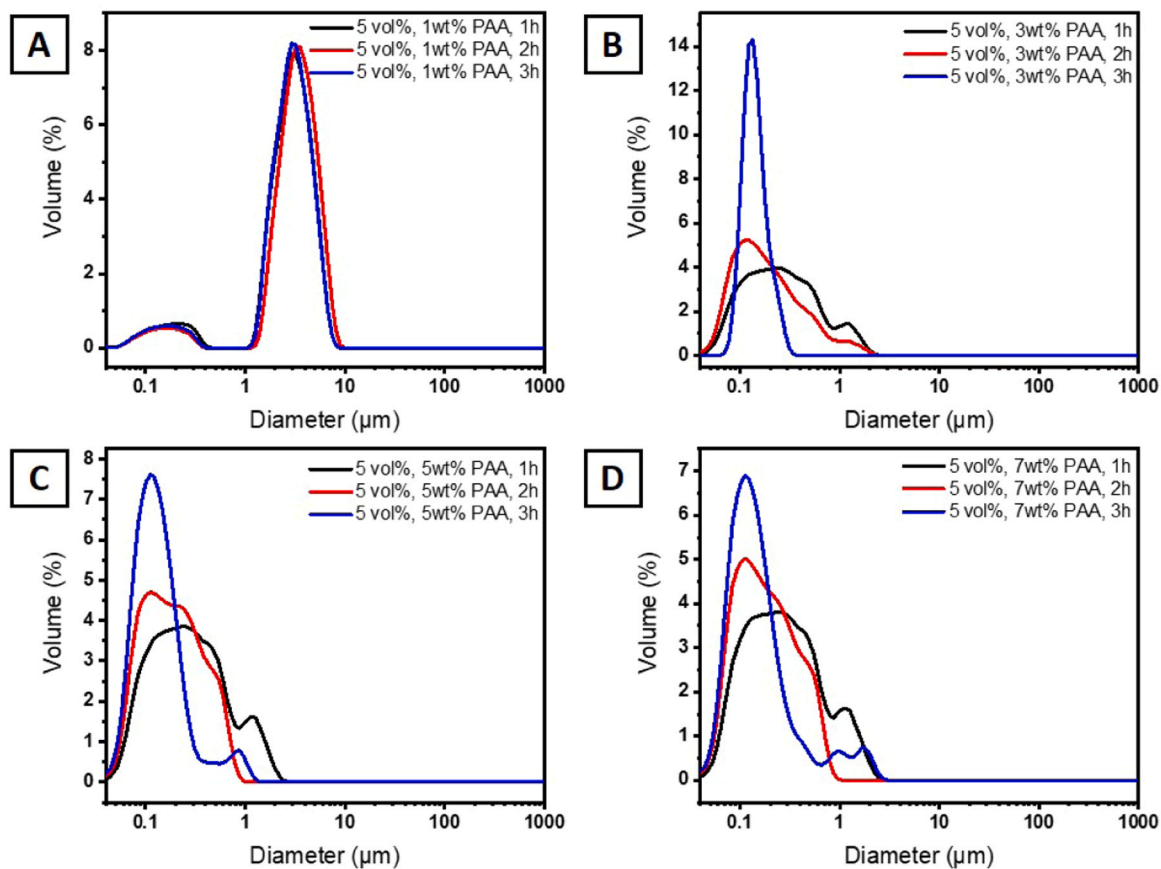
<https://doi.org/10.1016/j.jeurceramsoc.2024.03.049>

Received 13 December 2023; Received in revised form 13 March 2024; Accepted 16 March 2024

0955-2219/© 2024 The Authors. Published by Elsevier Ltd. This is an open access article under the CC BY license (<http://creativecommons.org/licenses/by/4.0/>).

Table 1Literature overview of conditions for pre-sintering and HIP of MgAl₂O₄ spinel and resulting transmittance, following [33].

Powder	S _{BET} [m ² /g]	Shaping	The conditions of pre-sintering	The conditions of HIP	Grain size [μm]	ρ _{th} [%]	RIT [%]	Ref.
Baikowski S30CR	25–28	Uniaxial powder compaction Colloidal slip casting	1700 °C/1 h 1650 °C/1 h	1800 °C/ 195 MPa/5 h	45–50	99.58 99.99	65 % (4 mm, 550 nm) ^c 80 % (4 mm, 550 nm) ^c	Ramavath 2014 [31]
Baikowski S30CR	25–28	Cold isostatic pressing	1550 °C /5 min	1550 °C /200 MPa/1 h	G = 1 μm G _M = 5 μm	100	60.2 % (@1.1 mm, 632.8 nm)	Maca 2007 [34]
Baikowski S30CR	25–28	Slipcasting	1550 °C /2 h	1450 °C /180 MPa/5 h	1.4	97.5	79.3 % (@1 mm, 550 nm)	Kim 2015 [29]
FSP ^a , Nanocerox	50	Cold isostatic pressing	1400 °C /80 h	1700 °C /200 MPa/3 h	0.45	99.9	77 % (@2 mm, 635 nm)	Goldstein 2008 [12]
FSP ^a	29–34	Freez drying, uniaxial pressing	1260 °C	1260 °C /200 MPa/15 h	0.34	>99.9 %	84 % (@3.7 mm, 640 nm)	Krell 2010 [13]
S30CR	25–28	Slipcasting	1550 °C/ 1 h	-	0.82	98.08 %	-	Talimian 2019 [35]
Baikowski Synthesis	n.a. ^d	SPS/CIP ^a	1575 °C/1 h	1500 °C/ 180 MPa/5 h	1.9	98 %	63 % (@1 mm, 550 nm)	Guo 2019 [33]
S25CR	21–24	Uniaxial + Cold Isostatic Pressing	Vacuum 1500 °C/2 h	1800 °C/ 190 MPa/ 10 h	28 + 125 ^b	~100 %	82 % (@2 mm, 400 nm)	Gajdowski 2017 [32]

^a FSP - flame spray pyrolysis, SPS - spark plasma sintering, CIP - cold isostatic pressing.^b two populations of grains.^c total or in-line transmittance: not specified.^d average particle size 180 nm.**Fig. 1.** Particle size distribution for 5 vol % aqueous suspensions for various milling times and different amounts of PAA with respect to the powder mass (A) 1 wt%, (B) 3 wt%, (C) 5 wt% and (D) 7 wt%.

example, provided that grain growth is controlled to prevent pore-grain boundary separation (e.g. formation of intragranular pores) as reported for spinel sintered in the air at 1600 °C [7]. These may subsequently coalesce at higher sintering temperatures, rapidly decreasing the optical properties [8]. Large intra-granular pores and small pore arrays

were observed in combination with abnormal grain growth in spinel samples after CIP and HIP at 1540 °C, whereby the pore arrays lead to significant local light scattering [9].

The effect of porosity on the real in-line transmittance can be calculated following Pecharroman and Mata-Osoro [10] using the

Table 2
Sample descriptions.

Sample name	Doping ^a	Pre-sintering temperature (°C)	HIP temperature (°C)
1500_3	-	1500	1300
Mg48	500 ppm Mg ²⁺	1500	1300
YMg54	250 ppm Y ³⁺ , 250 ppm Mg ²⁺	1500	1300
1500_2	-	1500	1350
Mg59	500 ppm Mg ²⁺	1500	1350
YMg60	250 ppm Y ³⁺ , 250 ppm Mg ²⁺	1500	1350
EuY50	250 ppm Eu ³⁺ , 250 ppm Y ³⁺	1500	1350
Eu61	500 ppm Eu ³⁺	1400	1400
Eu34	500 ppm Eu ³⁺	1500	1400
Y46	500 ppm Y ³⁺	1500	1400
EuMg52	250 ppm Eu ³⁺ , 250 ppm Mg ²⁺	1500	1400
EuY51	250 ppm Eu ³⁺ , 250 ppm Y ³⁺	1500	1400
EuYMg57	167 ppm Eu ³⁺ , 167 ppm Y ³⁺ , 167 ppm Mg ²⁺	1500	1400

^a By cationic ratio (Mg²⁺ + Al³⁺).

following equation, based on the Rayleigh scattering approximation:

$$\gamma_{\text{pores}} = 32 \frac{\phi_{\text{pores}} \pi^4 a_p^3}{\lambda_0^4} \left(\frac{n^2 - 1}{n^2 + 2} \right)^2 \quad (4)$$

with ϕ_{pores} – the pore volume fraction, a_p – the characteristic pore size (radius), λ_0 – the incident light wavelength (in vacuum) and n – the refractive index of the material (e.g., MgAl₂O₄ spinel).

Using fine powders has benefits in terms of sintering behaviour, as the increased excess surface energy leads to a lowering of the required sintering temperatures, e.g., use of MgAl₂O₄ particles with a $d_{n,50}$ of 5–6 nm allowed achieving relative densities over 95 % after only 20 min of sintering at 1300 °C [11]. For comparison, a powder with a mean particle size of 840 nm has been reported to only reach a density of 81 % after sintering for 4 hours at 1320 °C [12]. For Hot Isostatic Pressing HIP, using spinel powder with the S_{BET} 14–21 m²/g has been reported to require a HIP temperature of 1750 °C to achieve a *RIT* of 83 % (at $\lambda = 640$ nm) with an average grain size reaching up to 19.4 μm , whilst a powder with a specific surface $S_{\text{BET}} = 30$ –33 m²/g only needed 1260 °C during HIP to reach similar *RIT* values (e.g. 84 %) with an average grain size of 0.3 μm [13]. Furthermore, using finer powders allows for refined microstructures [14], which in return improves the mechanical properties of the final parts [15,16]. For example, a hardness and flexural strength of 16.5 GPa and 330 MPa, respectively, have been reported for spinel with the average grain size 0.14 μm , which were reduced to 12.9 GPa and 155 MPa, respectively, when increasing the average grain size to 25 μm [17]. Reports also suggest that abnormal grain growth may occur when sintering spinel above 1600 °C, leading to trapped intragranular pores [7]. One of the possible strategies to control grain boundary mobility and thus avoid intragranular pores is doping with elements that segregate at the grain boundaries and reduce its mobility by the solute drag effect. In the absence of dopant-induced liquid or secondary phase formation, the solute drag may improve the in-line transmittance by retarding grain growth, which prevents pore-grain boundary separation, and by promoting densification. Indeed, pore-grain boundary separation may occur when the velocity of pore movement is lower than grain boundary mobility [18]. The minimum grain size for pore-grain boundary separation G^* depends on the diffusion coefficients [19,20]:

$$G^* = \sqrt{\frac{\beta^4 \pi^3 D_s \delta_s \Omega}{16 D_b^+ a^2}} \quad (5)$$

with β – constant depending on the boundary curvature, D_b^+ – the atom diffusion coefficient, D_s – the surface diffusion coefficient, a^2 – the atom area, δ_s – the thickness of the diffusion surface and Ω – the atomic volume. The equation above illustrates that decreasing D_b^+ is favorable to prevent pore-grain boundary separation by increasing G^* .

For example, grain boundary segregation and, thus, grain growth inhibition was presented for yttrium doping [7,21], as well as improvement of the fracture toughness [22]. Dopants may also affect the sintering temperatures and densification rates. For instance, Mg²⁺ excess introduces oxygen vacancies associated with higher densification rates [23]. Reduction of sintering activation energy was also achieved by Mn²⁺ doping [24]. However, dopant solubility in spinel is relatively low and secondary phase precipitation occurs at higher doping levels [25, 26]. The levels depend on the grain boundary area as well as the bulk solubility and grain boundary segregation of the doping elements. From atomistic modelling results considering La³⁺, Y³⁺, Gd³⁺, La³⁺ and Zr⁴⁺ doping, La³⁺ has been reported to show the strongest grain boundary segregation for all investigated MgAl₂O₄ surfaces, which correlates with its large cationic radius size [27].

A review of reported spinel transmittance values including their shaping methods and sintering conditions is presented in Table 1. All studies used spinel powders with primary particle sizes in the 20 nm to 120 nm range. Although advantageous for lowering the sintering temperatures, the use of such small particles poses challenges during the processing [9,13,28,29], especially for MgAl₂O₄ which reacts with water due to its basic nature [30]. Not only the sintering conditions but also the method of shaping has an impact on the final density and thus optical properties. Indeed, higher sintering temperatures are required to obtain densities above 99 % for pellets prepared by spray drying and uniaxial powder compaction compared to parts prepared by slipcasting, which yields higher green body densities and typically higher transmittance values [31]. Pronounced grain growth has been particularly reported after HIP at 1800 °C [31,32]. The absence of birefringence, however, allowed reaching transmittance values close to the theoretical maximum, even with grain sizes of approx. 28 μm and 125 μm [32].

Considering the literature review and the objectives of the present study, the following doping elements were chosen to investigate their effect on slip-casted MgAl₂O₄ spinel samples:

- **Europium Eu³⁺** for its reported complex ion transitions (abrupt changes in the grain boundary structure and thus mobility) in magnesium aluminate spinel [36,37]
- **Yttrium Y³⁺** for its different cationic radius compared to Eu³⁺ with expected differences in its segregation and accommodation behavior, reducing the grain boundary energy by segregation and inhibiting grain coarsening [21]
- **Magnesium Mg²⁺** for introducing oxygen vacancies in the lattice, which often lead to improved diffusion and densification rates [23].

The goal of the study is to understand how Eu³⁺, Mg²⁺, and Y³⁺ ions affect the sintering path and microstructural development for MgAl₂O₄ spinel in order to promote sintering and densification and thereby achieve transparent spinel, ideally without HIP.

2. Experimental

2.1. Materials and methods

The powder used in this study was MgAl₂O₄ (S25CR, Baikowski, France) with a specific surface $S_{\text{BET}} = 23.1$ m²/g, $d_{v,50} = 0.2$ –0.3 μm and ≥ 99 % spinel crystal phase, according to the supplier data sheet. For proper deagglomeration of the powder, the 50 % solution of PAA 5000

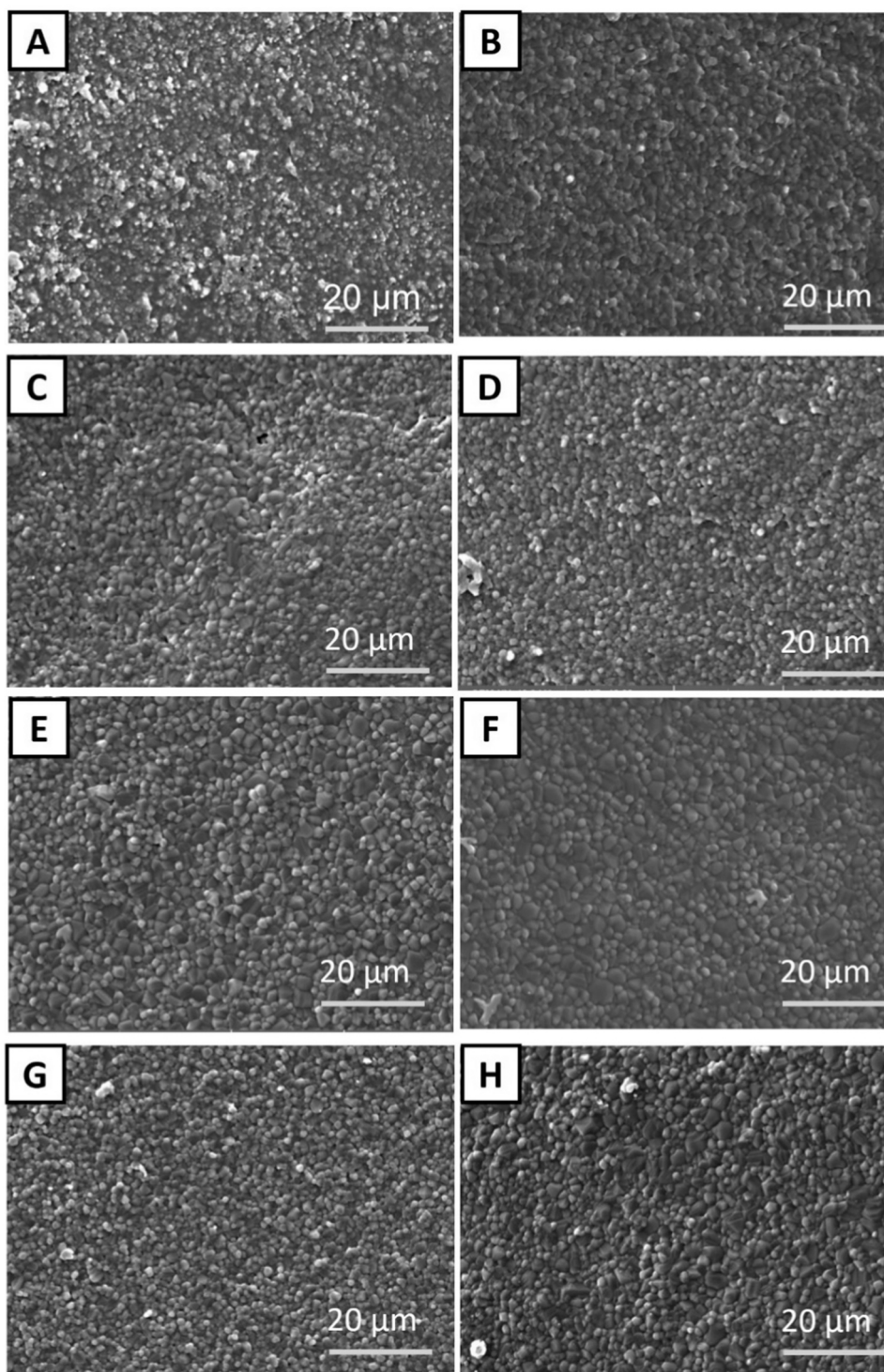


Fig. 2. SEM after pressureless sintering in 1400 °C for (A) pure spinel and doping: (B) Eu 500 ppm, (C) Mg 500 ppm, (D) Y 500 ppm, (E) Eu-Mg 250–250 ppm, (F) Eu-Y 250–250 ppm, (G) Mg-Y 250–250 ppm, (H) Eu-Y-Mg 167–167–167 ppm.

in water (Polysciences, USA) and NH_3 solution of 25 % (Roth, Switzerland) were used. The following salts were used for preparation of solutions for the doping process: $\text{Eu}(\text{NO}_3)_3 \cdot 5\text{H}_2\text{O}$ (Sigma Aldrich, Germany), $\text{Y}(\text{NO}_3)_3 \cdot 6\text{H}_2\text{O}$ (Sigma Aldrich, Germany) and $\text{Mg}(\text{NO}_3)_2 \cdot 6\text{H}_2\text{O}$ (Sigma Aldrich, Germany).

Planetary ball milling (Retsch, Germany) with alumina jars and balls (1 and 3 mm \varnothing) was used at 300 RPM and different milling times for the slurry preparation. Hereby, the powder to ball ratio was equal to 1:1 (1 mm \varnothing):0.7 (3 mm \varnothing).

The particle size distribution was performed by static light scattering (LS 13320, Beckman Coulter, USA) using water as a dispersing medium and Mie scattering as a model for the size calculation.

Pressure-less sintering was carried out in the Nabertherm furnace, (Germany LHT 04/17) with the maximum sintering temperature of 1750 °C and 4 L volume.

For the final densification of pure and doped spinel samples, Hot Isostatic Pressing (EPSI HIP 400–77*150 GM, EPSI, Temse, Belgium) was used with the following conditions:

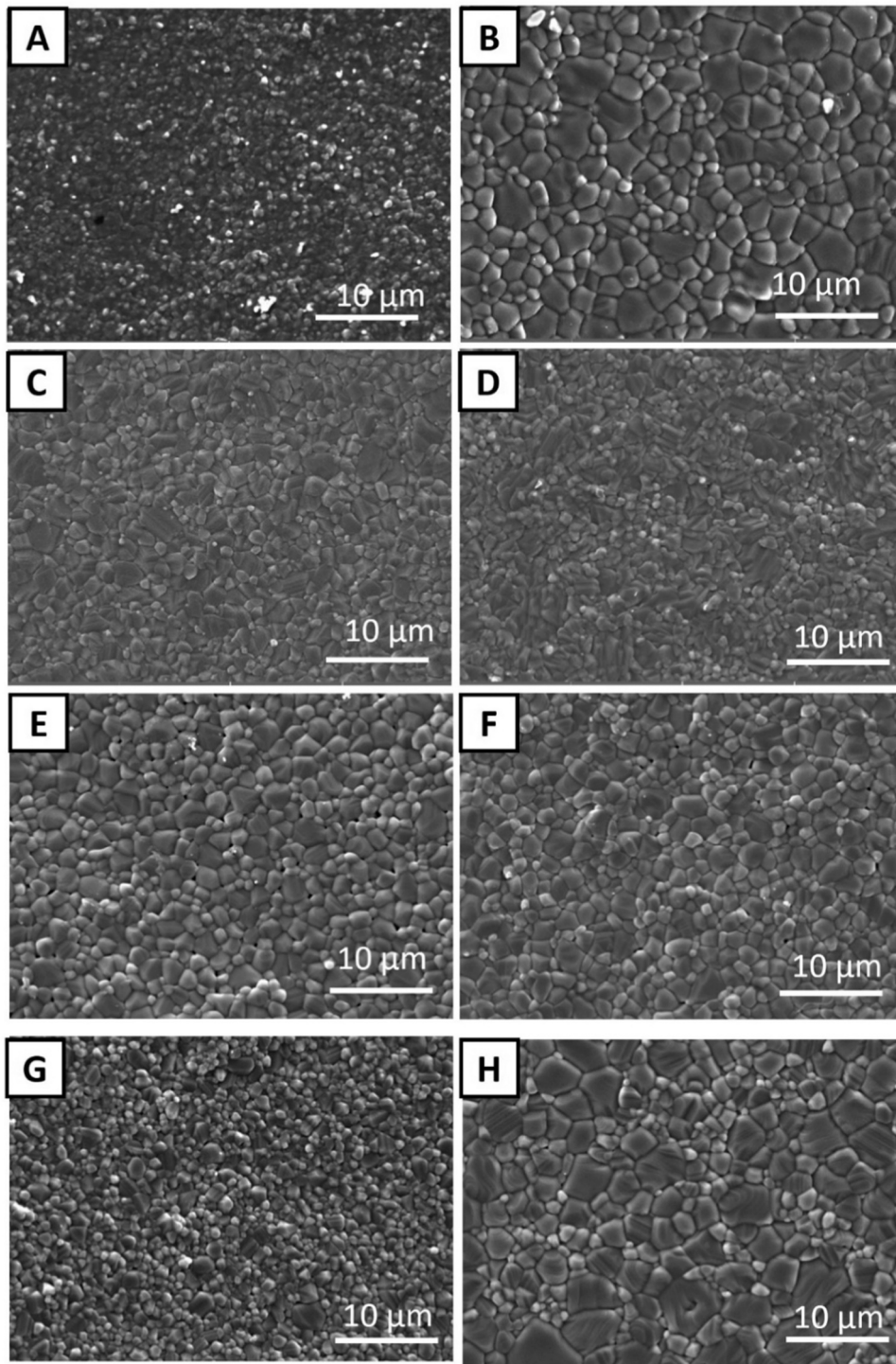


Fig. 3. SEM after pressureless sintering in 1500 °C for (A) pure spinel and doping: (B) Eu 500 ppm, (C) Mg 500 ppm, (D) Y 500 ppm, (E) Eu-Mg 250–250 ppm, (F) Eu-Y 250–250 ppm, (G) Mg-Y 250–250 ppm, (H) Eu-Y-Mg 167–167–167 ppm.

- 10 K/min; 1300 °C; 4 h; 200 MPa
- 10 K/min; 1350 °C; 4 h; 200 MPa
- 10 K/min; 1400 °C; 4 h; 200 MPa

The microstructure of sintered parts was analyzed by an SEM microscope (Vega Plus 5136 MM, Tescan, United Kingdom) equipped with an EDX detector.

The crystal structure was evaluated using X-ray diffractometer PANalytical X'Pert PRO θ -2 θ with a Cu $K\alpha_1$ radiation source. Measurements were performed between 20 and 80°. Phase identification

was completed using the X'Pert HighScore Plus software database. The crystalline size was calculated based on the Scherrer equation.

The density of sintered samples was evaluated following Archimedes' principle using an A6204 DeltaRange® balance (Mettler Toledo, Switzerland). The mass of the dried sample was recorded (m_1). To eliminate air and provoke pore penetration by water, the sample was immersed in distilled water and kept under a vacuum until bubbling stopped. After 24 hours of soaking, the mass of the sample was measured in water (m_2) and in air (m_3) after drying the surface to remove any excess surface water.

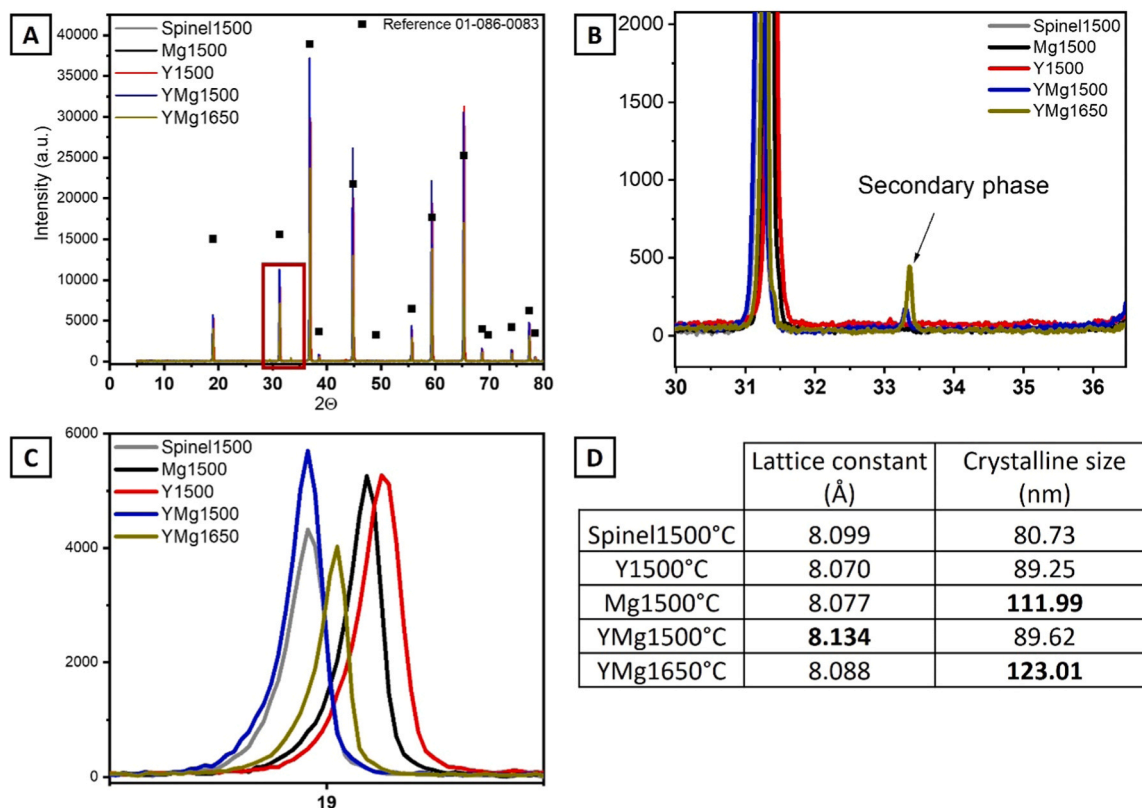


Fig. 4. XRD patterns for samples after pressureless sintering at 1500 °C: pure spinel, Mg-doped spinel, Y-doped spinel, YMg-doped spinel and sintered at 1650 °C YMg-doped spinel (A) XRD pattern comparison with the spinel reference, (B) secondary phase reflex, (C) shifts in the peak position and width, (D) table with calculated lattice constant and crystalline size.

A Jasco V-670 UV-vis-NIR double beam spectrometer with a 150 mm integrating sphere was used for the transmittance T and reflectance R measurement of pellets with a thickness of around 3 mm. The $T(\lambda)$ and $R(\lambda)$ spectra were measured in a wavelength range of 220–2200 nm. By using different measurement configurations, the integrating sphere enables recording the total, in-line and diffuse spectra separately. The analysis of diffuse transmittance T_{diff} and diffused reflectance R_{diff} allows determination of the contributions of light scattering.

2.2. Sample preparation

To optimize the dispersing concentration, deionized water was mixed with the required amount of the NH_3 solution, followed by PAA addition to obtain a ratio of NH_3 to AA (acrylic acid groups) of 1.5, before addition of the spinel powder under constant mixing with an IKA stirrer to obtain a 5 vol % suspension.

Knowing the critical importance of powder deagglomeration for the final density maximization, the milling process was particularly optimized. The impact of various PAA dosage (1 wt%, 3 wt%, 5 wt% and 7 wt% with respect to the powder mass) on the particle size distribution was examined for 5 vol % spinel slurry (Fig. 1). For 1 wt% of PAA (Fig. 1A), adjusting the milling time between 1 and 3 hours does not allow achieving a fully de-agglomerated slurry state. An increase of the PAA concentration to 3 wt% (Fig. 1B) allowed reaching a monomodal particle size distribution after 3 hours of milling. A further increase of the PAA concentration (5 wt% and 7 wt%) instead resulted in the presence of bigger agglomerates (Fig. 1 C, D). This could be a result of bridging effects between an increasingly large network of free polymers [38] or ammonium polyacrylate modifying the ionic strength compressing the double-layer [39]. Accordingly, 3 wt% of PAA and 3 hours of milling were chosen as the optimum to achieve full de-agglomeration.

Finally, the slurry concentration was increased to 20 vol %.

Slip-casting of spinel was performed in silicone molds placed on a gypsum plaster covered with a cellulose filter paper. After covering and 3 days of drying, samples were removed from the mold, placed in an open crucible on a corundum sand for PAA removal and calcination, according to the following two-step heating program: heating at 0.5 °C/min to 600 °C with a dwell of 120 min, then heating at 5 °C/min to 800 °C with a dwell of 30 min. After calcination, the density of green bodies was measured using the generalized Archimedes method and the pore volume calculated comparing the measured density with the theoretical density of spinel (3.58 g/cm³). After drying the samples in an oven at 120 °C in air overnight, the samples were doped by pipetting an equivalent of the pore volume of aqueous nitrate solutions (prepared by dilution of ICP-OES titrated stock solutions) with concentrations needed to achieve a doping level of 500 ppm by cation ratio Mg^{2+} and Al^{3+} (Table 2), dried and sintered in a box furnace at 1400 °C or 1500 °C for 4 hours. All types of samples were subjected to a post-HIP process at 1350 °C and afterwards optically evaluated to define the subsequent experimental trials according to the following protocol: dopant strategies having a translucent appearance after this initial post-HIP trial were selected for another post-HIP trial at lower temperature (1300 °C); dopant strategies yielding a milky or slightly yellowish (assuming this being the consequence of microporosity) appearance were selected for another post-HIP trial at higher temperature (1400 °C). For the transmittance measurement, only samples with translucent/ transparent properties were chosen. The final set of samples is presented in Table 2.

3. Results and discussion for pressure-less sintering before HIP

3.1. SEM and XRD at 1400 °C and 1500 °C

No significant microstructural changes could be observed in pure and

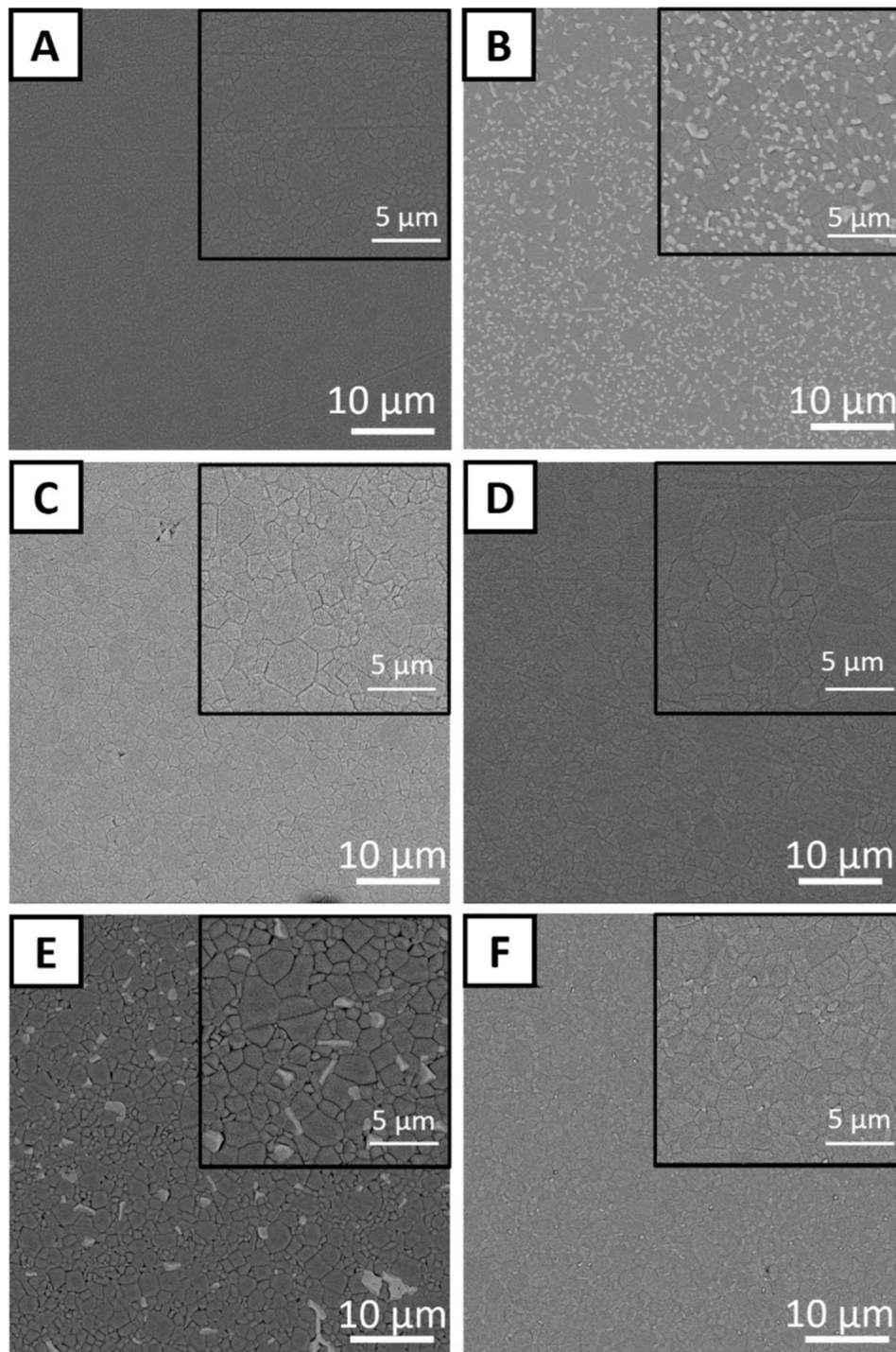


Fig. 5. SEM images after HIP at 1400 °C (A) Eu61, (B) Eu34, (C) Y46, (D) EuMg52, (E) EuY51 and (F) EuYMg57.

doped spinel after pre-sintering at 1400 °C (Fig. 2). In all cases, the microstructure is homogenous without the presence of abnormally grown or excessively large grains.

After sintering at 1500 °C, microstructural changes start to be noticeable (Fig. 3): Whilst the addition of Eu (Fig. 3B), Eu-Mg (Fig. 3E), Eu-Y (Fig. 3F) and Eu-Y-Mg (Fig. 3H) leads to more significant grain growth, the addition of Mg (Fig. 3C), Y (Fig. 3D) and Y-Mg (Fig. 3G) allows limiting grain growth compared to the Eu-(co)-doped ones. The increased grain growth observed for Eu-doped samples compared to undoped spinel may be a result of complexion transitions, which may lead to higher grain boundary mobility irrespective of the solute drag

effect. Indeed, a complexion transition for Eu-doped spinel has already been previously reported, occurring around 1480 °C with 4-hour sintering dwell times [36,40,41]. Alternatively, the generation of a liquid phase at the grain boundaries may also lead to similar results [9].

To analyse the phase purity and possible changes in lattice constant and crystallite size, the XRD data were collected for some samples sintered at 1500 °C and one sintered in 1650 °C (Fig. 4). High purity spinel phase could be confirmed for most of the samples (Fig. 4A) (within the detection limit of XRD). Only for YMg (sintered at both 1500 °C and 1650 °C) could a peak that can be associated with the precipitation of a secondary phase be observed around $2\theta = 33.4^\circ$ (Fig. 4B). For YMg1500

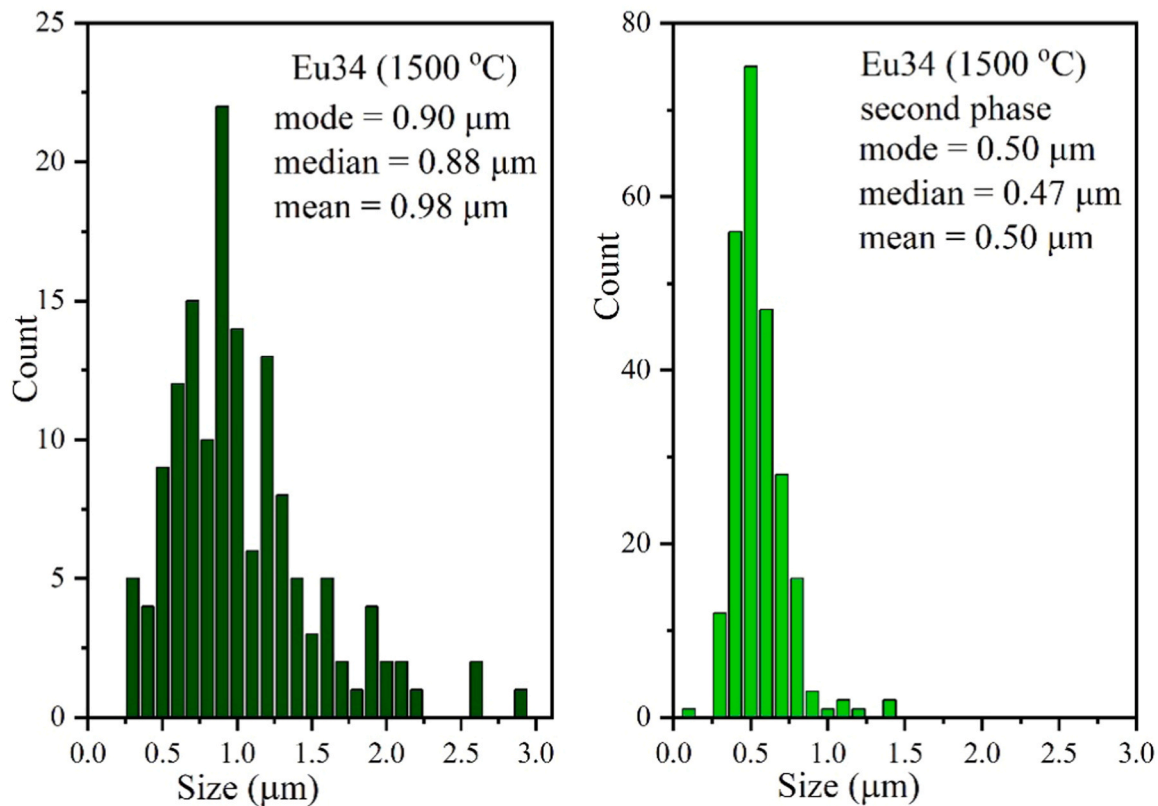


Fig. 6. Grain size distribution for sample Eu34.

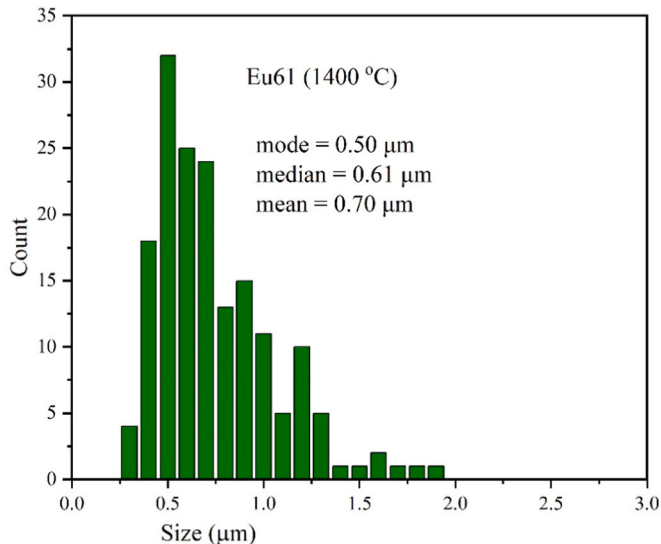


Fig. 7. Grain size distribution for sample Eu61.

and YMg1650 samples, a $Y_3Al_5O_{12}$ phase (reference no. 01-090-1264) was found in addition to the $MgAl_2O_4$ spinel phase (reference no. 01-086-0083). Both roentgenograms are of high quality and are characterized by a very high number of counts. For the YMg1500 sample, the intensity ratio of the highest intensity reflections after background subtraction is equal to $Y_3Al_5O_{12} : MgAl_2O_4 = 0.011$. An analogous analysis of the YMg1650 sample yields 0.005. Therefore, it can be seen that the contribution of the additional $Y_3Al_5O_{12}$ phase is very small. Considering that the $Y_3Al_5O_{12}$ phase could only be detected for both samples doped with Y-Mg (Y^{3+} and Mg^{2+}) and not for single doping with

the same (only Y^{3+} or only Mg^{2+}), the formation of a secondary phase might be related to a synergistic doping effect, the exact investigation of which is beyond the scope of this study. It shall be noted, however, that magnesium deficiency at grain boundaries has been reported in pure spinel [42,43], leading to the assumption that magnesium co-doping might significantly influence the grain boundary chemistry. XRD analysis also reveals slight shifts in the position of the peak around $2\theta = 19^\circ$ (Fig. 4C) which is indicative of a lattice constant change between the samples. The lattice constant and crystallite size were calculated and the average value for all peaks is presented in Fig. 4D. There is a slight increase in the crystallite size for Y-doped and YMg-doped spinel sintered at 1500 °C. Larger crystallite sizes were measured for the Mg-doped spinel sintered at 1500 °C and the YMg-doped spinel sintered at 1650 °C. A minor decrease of the lattice constant could be observed for Mg- and Y-doped spinel, which in the case of Mg-doping could be associated with the formation of charge compensating oxygen vacancies. YMg-doping, however, causes a slight increase of the lattice constant, which decreases after sintering at higher temperatures where the formation of a secondary phase depletes the doping element concentration in the structure.

4. Results and discussion after HIP

4.1. SEM observations after post-HIP

After post-HIP at 1350 °C, no substantial difference could be observed in terms of microstructure homogeneity and grain size for undoped (SD Fig. 1) and Mg-doped spinel. However, for EuY- and YMg-doped spinel, some inhomogeneous grain growth was observed within an otherwise homogeneous and fine microstructure.

To analyse the chemical homogeneity and the composition of white precipitations observed on the micrographs of YMg-doped spinel, EDX analysis was carried out. After post-HIP at 1300 °C, yttrium spots were detected and attributed to the secondary phase precipitation (SD Fig. 3).

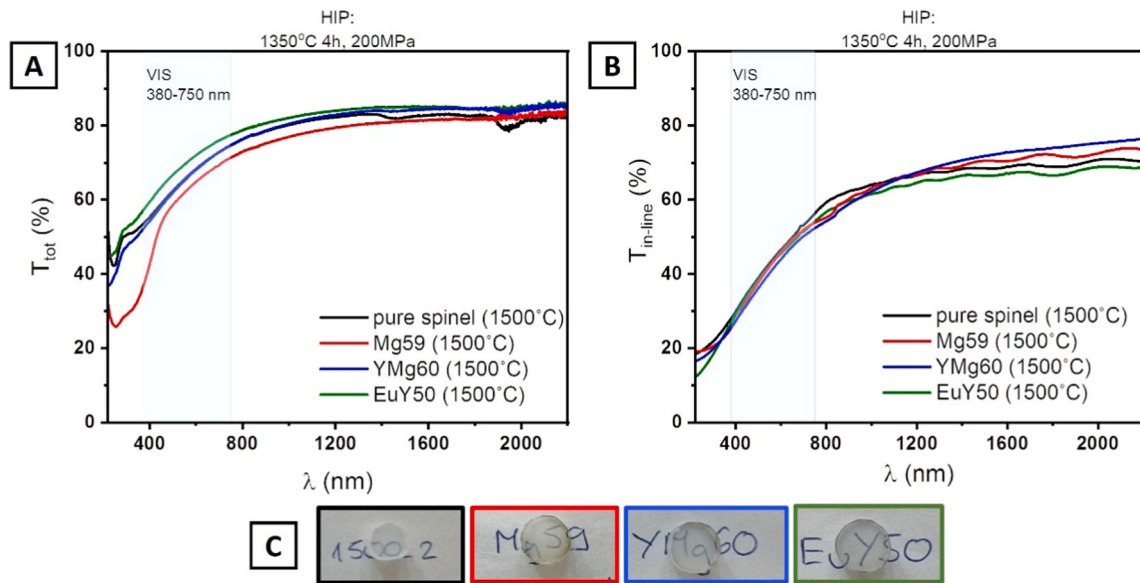


Fig. 8. Transmittance measurement after HIP at 1350 °C and 200 MPa (A) total and (B) in-line transmittance, and (C) pictures of polished pellets. Pre-sintering temperatures are given in brackets.

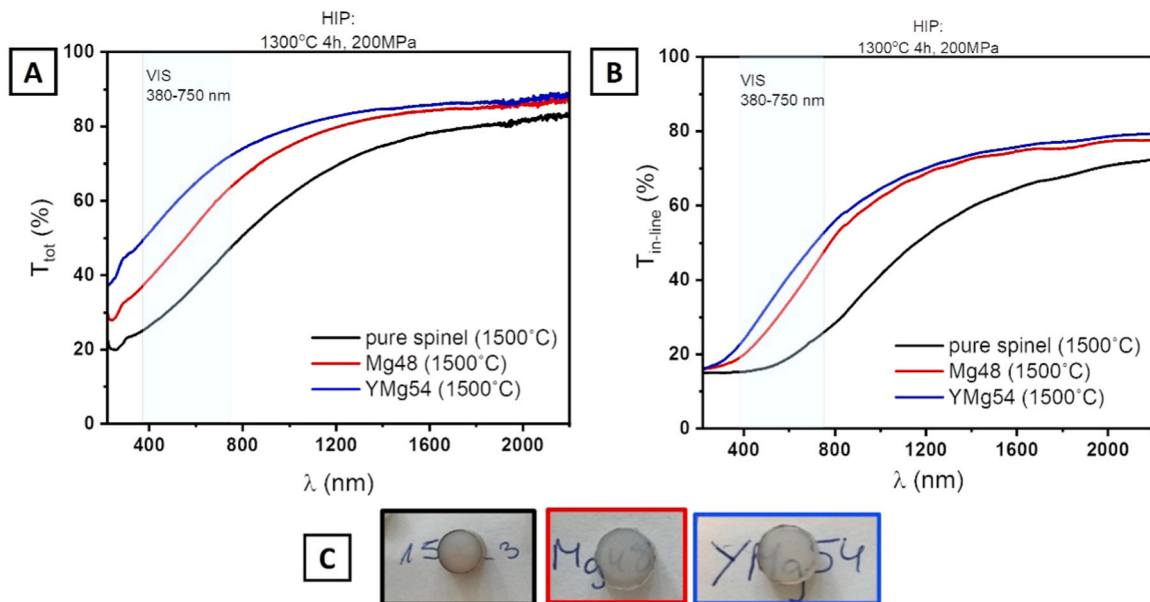


Fig. 9. Transmittance measurement after HIP at 1300 °C and 200 MPa (A) total and (B) in-line transmittance, and (C) pictures of polished pellets. Pre-sintering temperatures are given in brackets.

After post-HIP at 1350 °C, white spots of the secondary phase were no longer detected at the grain boundaries (SD Fig. 3), which could be the result of increased solubility at higher sintering temperature, such as reported for Ca in alumina [44]. The presence of precipitates leads to additional scattering effects, lowering the transmittance in this sample as discussed in the next section.

The microstructure after post-HIP at 1400 °C is presented in Fig. 5. White precipitations of secondary phases were observed for the following samples: Eu-doped and pre-sintered at 1500 °C (Eu34), EuY-doped and pre-sintered at 1500 °C (EuY51) and EuYMg doped and pre-sintered at 1500 °C (EuYMg57), whereas the highest precipitation level was observed for the sample Eu34. Sample Eu61 shows a fine-grain microstructure. A rather bimodal microstructure is observed for samples Eu34 (Fig. 5B), Y46 (Fig. 5 C) and EuMg52 (Fig. 5 D), with the latter showing the most substantial abnormal grain growth. Although difficult

to evaluate on thermally etched micrographs, sample EuY51 appears to have a higher level of porosity (Fig. 5 E).

For the two Eu-doped samples, the grain size distribution was compared (Fig. 6, Fig. 7). In the case of pre-sintering at higher temperature, the median shifted to 0.88 μm compared to 0.61 μm at lower temperature. Bigger grains up to 3 μm are present in the sample Eu34 (pre-sintered at 1500 °C). In addition, for the sample pre-sintered at 1500 °C, precipitation of a fine secondary phase appeared. The reason for this was not further investigated, but could be related to a complexion transition, changing the grain boundary structure and solubility of the element at grain boundaries. A similar effect was reported for Ca-doped spinel, where abnormal grain growth and secondary phase precipitation led to a decrease in-line transmittance after HIP at 1500 °C compared HIP at 1450 °C [18]. Indeed, grain growth reduces the total grain boundary area/density, reducing the amount of doping elements

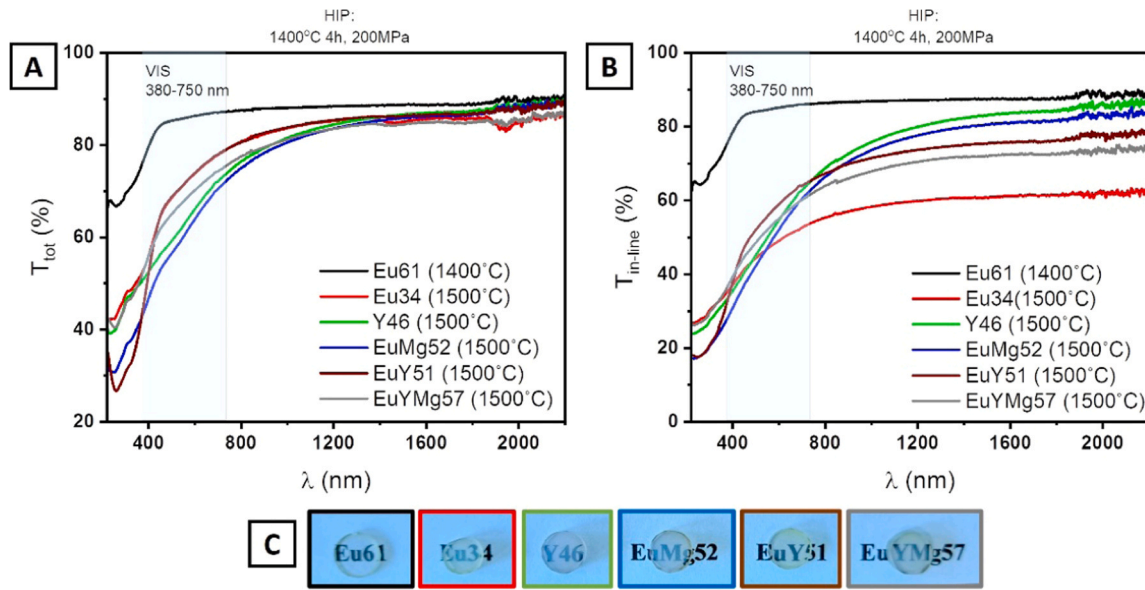


Fig. 10. Transmittance measurement after HIP in 1400 °C and 200 MPa (A) total and (B) in-line transmittance, (C) pictures of polished pellets. Pre-sintering temperatures are given in brackets.

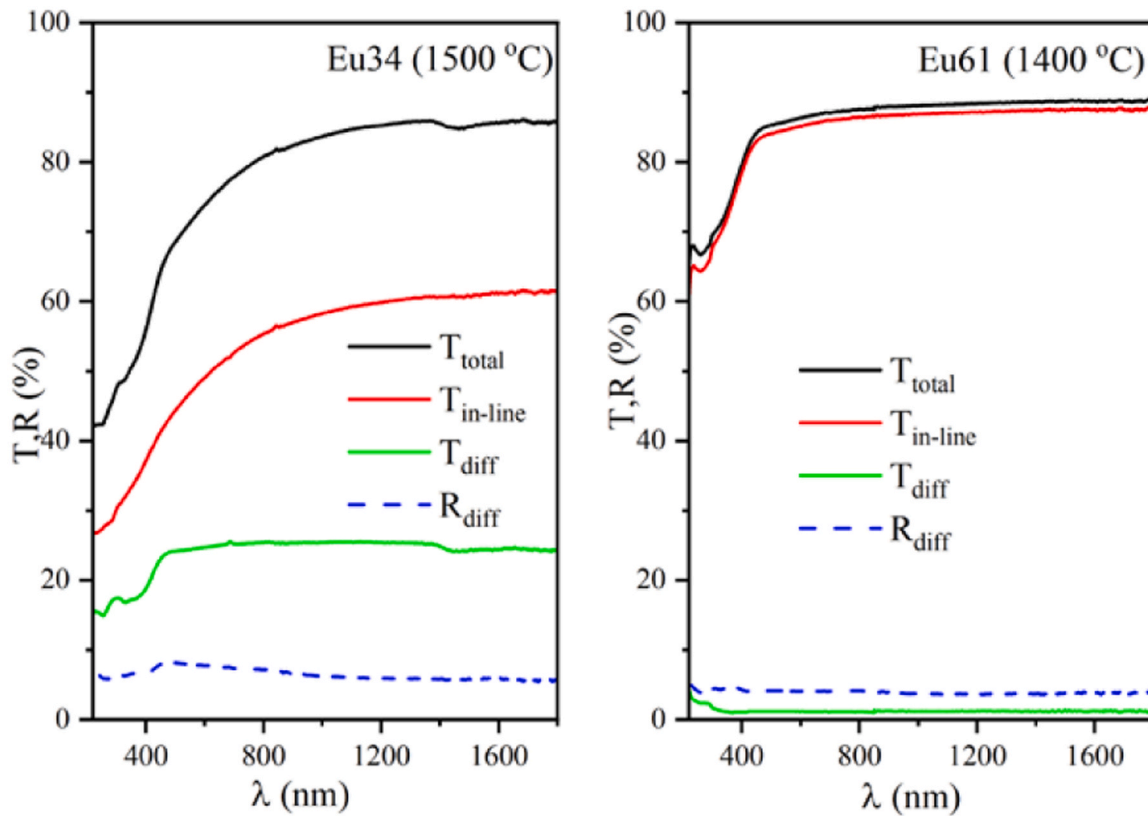


Fig. 11. Comparison of transmittance (total, in-line and diffusive) and reflectance diffusive for Eu-doped samples pre-sintered at 1400 °C and 1500 °C.

that may be accommodated before secondary phase precipitation.

4.2. Optical measurements after post-HIP

In the visible light range, post-HIP at 1350 °C improves the total transmittance only for EuY-doped spinel (Fig. 8A) compared to pure spinel. For YMg-doping, instead, no significant changes can be observed and for Mg-doping even a slight decrease in the total transmittance

compared to undoped spinel occurs. When considering the in-line transmittance, all samples have a similar performance within the visible range (Fig. 8 B).

Post-HIP at 1300 °C reveals more significant doping effects (Fig. 9). For instance, at $\lambda = 750$ nm a real in-line transmittance increases from 26 % (undoped spinel) to 48 %, and 53 % is observed for Mg-doped and YMg-doped spinel, respectively. The total transmittance was improved from around 48% to 72% for YMg-doped spinel at the same wavelength

Table 3

Comparison of achieved transparency with other authors.

Data							Calculated for d = 1 mm
Reference	λ (nm)	T_{\max}^* (%)	RIT (%)	d (mm)	γ , tot (nm^{-1})	ρ (%)	RIT (%)
Ramavath [31]	550	87	80	4	$2.10 \cdot 10^{-8}$	99.99	<u>85.2</u>
Maca [34]	632.8	87	60.2	1.1	$3.35 \cdot 10^{-7}$	100	<u>62.2</u>
Kim [29]	550	87	79.3	1	$9.27 \cdot 10^{-8}$	97.5	<u>79.3</u>
Goldstein [12]	635	87	80	2	$4.19 \cdot 10^{-8}$	99.9	<u>83.4</u>
Krell [13]	640	87	84	3.7	$9.48 \cdot 10^{-9}$	99.9	86.2
Guo [33]	550	87	63	1	$3.23 \cdot 10^{-7}$	98	<u>63.0</u>
Gajdowski [32]	400	87	82	2	$2.96 \cdot 10^{-8}$	100	<u>84.5</u>
This study, pure spinel	500	87	39	3	$2.68 \cdot 10^{-7}$	99.11	66.5
This study, Eu61	500	87	84.1	3	$1.13 \cdot 10^{-8}$	99.92	86.0

 T_{\max} – the maximum theoretical transmittance.**Table 4**Calculated characteristic pore size for samples after HIP for $\lambda = 400$ nm and spinel refractive index $n = 1.7368$.

Pre-sintering Temp. (°C)	HIP Temp (°C)	Sample	RIT (%)	γ_{tot} (nm^{-1})	ρ_{rel} (%)	φ_{pores} (%)	a_p (nm)
1500	1300	1500_3	15.30	$5.72 \cdot 10^{-7}$	~100 % ^b	<0.01	>66.5
1500	1300	Mg48	19.92	$4.84 \cdot 10^{-7}$	99.71	0.29	20.5
1500	1300	YMg54 ^a	23.96	$4.22 \cdot 10^{-7}$	~100 % ^b	<0.01	>60.2
1500	1350	1500_2	29.88	$3.48 \cdot 10^{-7}$	99.11	0.89	12.6
1500	1350	Mg59	27.25	$3.79 \cdot 10^{-7}$	99.98	0.02	46.4
1500	1350	YMg60	27.30	$3.79 \cdot 10^{-7}$	99.78	0.22	20.5
1500	1350	EuY50	28.89	$3.60 \cdot 10^{-7}$	99.97	0.03	37.4
1400	1400	Eu61	78.52	$2.64 \cdot 10^{-8}$	99.28	0.72	5.7
1500	1400	Eu34	37.15	$2.76 \cdot 10^{-7}$	99.43	0.57	13.5
1500	1400	Y46	35.48	$2.91 \cdot 10^{-7}$	99.63	0.37	15.9
1500	1400	EuMg52	30.87	$3.38 \cdot 10^{-7}$	99.33	0.67	13.6
1500	1400	EuY51	37.87	$2.70 \cdot 10^{-7}$	99.15	0.85	11.7
1500	1400	EuYMg57	39.31	$2.57 \cdot 10^{-7}$	99.56	0.44	14.3

^a Secondary phase precipitation contributes to RIT reduction, so the calculation of the characteristic pore size has a higher inaccuracy.^b for characteristic pore size calculation, the density was assumed as 99.99 %.

but the values remain below those obtained after HIP at 1350 °C.

These agree with the assumption that when post-HIP is used to maximize the optical properties of spinel, doping has no significant effect, provided no intra-granular pores are formed, given that the optical properties solely depend on the residual porosity and are independent of the grain size. The same, however, does not hold when the mechanical properties are also considered.

For the highest evaluated post-HIP temperature (1400 °C), a substantial improvement of transmittance in the visible light range was measured for Eu-doping pre-sintered at 1400 °C (Eu61, Fig. 10). A transmittance as high as 84 % could be measured, approaching the theoretical limit of 87 %. In contrast, pre-sintering at 1500 °C leads to a significant reduction in in-line transmittance compared to the other samples (Eu 34, Fig. 11 B), which could be explained by the significant secondary phase precipitation confirmed by SEM-EDX analysis. All other samples do not exceed 65 % in real in-line transmittance in the visible light range and show significant differences in the IR range.

The transmittance spectra, recorded both in classical (in-line) configuration as well as an integrating sphere, are presented in Fig. 11 for Eu-doped samples. The total transmittance T_{total} does not differ from $T_{\text{in-line}}$ when the sample Eu-61 was pre-sintered at temperature 1400 °C. In this case the diffuse signal T_{diff} is small. Large differences between T_{total} and $T_{\text{in-line}}$ develop for higher pre-sintered temperature, 1500 °C (Eu-34). The high diffuse transmittance T_{diff} for sample Eu-34 is related to the light scattering centres and can be correlated with the presence of a second phase observed by SEM (Fig. 5B and Fig. 6).

The comparison of achieved transparency with the values available in the literature is presented in Table 3 with RIT calculated for a sample thickness of 1 mm. Eu doping for presented sintering conditions (pre-sintering at 1400 °C and HIP at 1400 °C for 4 hours with 200 MPa) and concentration of 500 ppm by cation ratio allows achieving a considerably improved transmittance, approaching the theoretical value for the relatively low sintering temperatures (1400 °C for both pre-sintering

and HIP), in comparison to 1800 °C [31] [32]. Only using very fine spinel powder with a particle size of 20–30 nm allowed to achieve RIT over 80 % [13] for a low HIP temperature of 1320 °C. For pure spinel, this value is significantly lower (only 66.5 %) for pre-sintering at 1500 °C and HIP at 1350 °C. This indicates the very promising potential of europium doping for spinel to achieve high transmittance for relatively low sintering temperatures.

4.3. Density and characteristic pore size calculation

The characteristic pore size for the measured porosity at 400 nm wavelength was calculated based on the Pecharroman model (Eq. 4) and presented in Table 4. For all samples, densities over 99 % were obtained, for pure spinel 1500_3 and YMg54 doped spinel approaching 100 %. Based on the model, slightly higher RIT after HIP at 1350 °C for pure spinel is related to smaller characteristic pore size, namely around 13 nm in comparison to 46 nm for Mg-doped spinel. For the highest evaluated HIP temperature (1400 °C), Eu doping in lower pre-sintering temperature (1400 °C) allows reduction of the characteristic pore size to 5.7 nm, in comparison to other samples after the same HIP temperature having the characteristic pore size in the range of 10–15 nm.

5. Summary and conclusions

Aiming ultimately for the additive manufacturing of transparent spinel ceramics, careful deagglomeration of a submicron starting powder allowed significant reduction of the sintering temperature compared to those more commonly reported in literature. Such careful colloidal processing is needed to explore the higher sintering activity of sub-micron powders and obtain defect-free ceramics without excessive grain growth.

For the presented pre-sintering and post-HIP conditions, RIT values approaching the theoretical limit were obtained for MgAl₂O₄ spinel

doped with europium (500 ppm by cationic ratio), pre-sintering above pore closure at 1400 °C and post-HIPing at 1400 °C. These conditions allowed achievement of a relatively fine microstructure without the need for alternative fast sintering techniques. Despite its cubic material system, co-doping with multivalent cations may be promising: a meaningful improvement in RIT was obtained after HIP at low temperatures, namely from 26 % for pure spinel to 53 % for YMg-doped spinel ($\lambda = 750$ nm, HIP at 1300 °C), highlighting the potential benefits to explore alternative co-doping strategies.

CRedit authorship contribution statement

Paulina Zubrzycka: Conceptualization, Data curation, Formal analysis, Investigation, Methodology, Project administration, Visualization, Writing – original draft. **Marta Radecka:** Formal analysis, Investigation, Methodology, Project administration, Resources, Supervision, Validation, Writing – original draft. **Thomas Graule:** Funding acquisition, Project administration, Resources, Supervision. **Anita Trenczek-Zajac:** Data curation, Formal analysis, Investigation, Methodology, Validation, Visualization. **Dariusz Zientara:** Investigation. **Michael Stuer:** Conceptualization, Methodology, Supervision, Validation, Writing – review & editing.

Declaration of Competing Interest

The authors declare that they have no known competing financial interests or personal relationships that could have appeared to influence the work reported in this paper.

Acknowledgment

This work was supported by the ‘Excellence initiative-research university’ for the AGH University of Science and Technology (MR, AT-Z) and by Empa’s Board of Directors.

Appendix A. Supporting information

Supplementary data associated with this article can be found in the online version at [doi:10.1016/j.jeurceramsoc.2024.03.049](https://doi.org/10.1016/j.jeurceramsoc.2024.03.049).

References

- [1] C. Pecharroman, G. Mata-Osoro, L.A. Diaz, R. Torrecillas, J.S. Moya, On the transparency of nanostructured alumina: Rayleigh-Gans model for anisotropic spheres, *Opt. Express* 17 (8) (2009) 6899–6912.
- [2] S. Hřibálová, W. Pabst, Light scattering and extinction in polydisperse systems, *J. Eur. Ceram. Soc.* 40 (3) (2020) 867–880.
- [3] M. Stuer, P. Bowen, Z. Zhao, Spark plasma sintering of ceramics: from modeling to practice, *Ceramics* 3 (4) (2020) 476–493.
- [4] A. Krell, J. Klimke, T. Hutzler, Transparent compact ceramics: Inherent physical issues, *Opt. Mater.* 31 (8) (2009) 1144–1150.
- [5] M. Stuer, P. Bowen, M. Cantoni, C. Pecharroman, Z. Zhao, Nanopore characterization and optical modeling of transparent polycrystalline alumina, *Adv. Funct. Mater.* 22 (11) (2012) 2303–2309.
- [6] J.H. Burnett, S.G. Kaplan, E.L. Shirley, P.J. Tompkins, J.E. Webb, High-index materials for 193 nm immersion lithography, in: *Optical Microlithography XVIII*, SPIE, 2005, pp. 611–621.
- [7] C.J. Ting, H.Y. Lu, Deterioration in the final-stage sintering of magnesium aluminate spinel, *J. Am. Ceram. Soc.* 83 (7) (2000) 1592–1598.
- [8] K. Hoggas, S. Benaissa, A. Cherouana, S. Bouheroum, A. Assali, M. Hamidouche, G. Fantozzi, Mechanical behavior of transparent spinel fabricated by spark plasma sintering, *Ceramics* 6 (2) (2023) 1191–1209.
- [9] A. Krell, T. Hutzler, J. Klimke, Defect strategies for an improved optical quality of transparent ceramics, *Opt. Mater.* 38 (2014) 61–74.
- [10] G. Mata-Osoro, J.S. Moya, C. Pecharroman, Transparent alumina by vacuum sintering, *J. Eur. Ceram. Soc.* 32 (11) (2012) 2925–2933.
- [11] J. Rufner, D. Anderson, K. van Benthem, R.H.R. Castro, R. Hay, Synthesis and sintering behavior of ultrafine (<10 nm) magnesium aluminate spinel nanoparticles, *J. Am. Ceram. Soc.* 96 (7) (2013) 2077–2085.
- [12] A. Goldstein, A. Goldenberg, Y. Yeshurun, M. Hefetz, Transparent MgAl₂O₄ spinel from a powder prepared by flame spray pyrolysis, *J. Am. Ceram. Soc.* 91 (12) (2008) 4141–4144.
- [13] A. Krell, T. Hutzler, J. Klimke, A. Potthoff, Fine-grained transparent spinel windows by the processing of different nanopowders, *J. Am. Ceram. Soc.* 93 (9) (2010) 2656–2666.
- [14] F.-S. Shiao, T.-T. Fang, T.-H. Leu, Effect of particle-size distribution on the microstructural evolution in the intermediate stage of sintering, *J. Am. Ceram. Soc.* 80 (2) (2005) 286–290.
- [15] A. Goldstein, Correlation between MgAl₂O₄-spinel structure, processing factors and functional properties of transparent parts (progress review), *J. Eur. Ceram. Soc.* 32 (11) (2012) 2869–2886.
- [16] A. Krell, J. Klimke, T. Hutzler, Advanced spinel and sub- μ m Al₂O₃ for transparent armour applications, *J. Eur. Ceram. Soc.* 29 (2) (2009) 275–281.
- [17] M. Sokol, S. Kalabukhov, R. Shneck, E. Zaretsky, N. Frage, Effect of grain size on the static and dynamic mechanical properties of magnesium aluminate spinel (MgAl₂O₄), *J. Eur. Ceram. Soc.* 37 (10) (2017) 3417–3424.
- [18] J.-M. Kim, H.-N. Kim, Y.-J. Park, J.-W. Ko, J.-W. Lee, H.-D. Kim, Microstructure and optical properties of transparent MgAl₂O₄ prepared by Ca-infiltrated slip-casting and sinter-HIP process, *J. Eur. Ceram. Soc.* 36 (8) (2016) 2027–2034.
- [19] R.J. Brook, Pore-grain boundary interactions and grain growth, *J. Am. Ceram. Soc.* 52 (1) (1969) 56–57.
- [20] S.-J.L. Kang, *Sintering: Densification, Grain Growth and Microstructure*, Elsevier, 2004.
- [21] M.M. Hasan, P.P. Dholabhai, S. Dey, B.P. Uberuaga, R.H.R. Castro, Reduced grain boundary energies in rare-earth doped MgAl₂O₄ spinel and consequent grain growth inhibition, *J. Eur. Ceram. Soc.* 37 (13) (2017) 4043–4050.
- [22] W. Cao, A. Kundu, Z. Yu, M.P. Harmer, R.P. Vinci, Direct correlations between fracture toughness and grain boundary segregation behavior in ytterbium-doped magnesium aluminate spinel, *Scr. Mater.* 69 (1) (2013) 81–84.
- [23] C.-J. Ting, H.-Y. Lu, Defect reactions and the controlling mechanism in the sintering of magnesium aluminate spinel, *J. Am. Ceram. Soc.* 82 (4) (1999) 841–848.
- [24] K. Nakajima, H. Li, N. Shlesinger, J.B. Rodrigues Neto, R.H.R. Castro, Low-temperature sintering of magnesium aluminate spinel doped with manganese: Thermodynamic and kinetic aspects, *J. Am. Ceram. Soc.* 103 (8) (2020) 4167–4177.
- [25] J. Liu, Z. Wang, H. Liu, X. Wang, Y. Ma, Effect of Y₂O₃ doping on the high-temperature properties of magnesia aluminate spinel refractories, *J. Aust. Ceram. Soc.* 56 (2) (2019) 389–394.
- [26] S.S. Balabanov, A.V. Belyaev, E.M. Gavrilshchuk, I.B. Mukhin, A.V. Novikova, O. V. Palashov, D.A. Permin, I.L. Snetkov, Fabrication and measurement of optical and spectral properties of the transparent Yb:MgAl₂O₄ ceramics, *Opt. Mater.* 71 (2017) 17–22.
- [27] M.M. Hasan, P.P. Dholabhai, R.H.R. Castro, B.P. Uberuaga, Stabilization of MgAl₂O₄ spinel surfaces via doping, *Surf. Sci.* 649 (2016) 138–145.
- [28] P. Zubrzycka, M. Radecka, T. Graule, M. Stuer, Metal cation complexes as dispersing agents for non-aqueous powder suspensions, *Ceram. Int.* 47 (13) (2021) 18443–18454.
- [29] J.-M. Kim, H.-N. Kim, Y.-J. Park, J.-W. Ko, J.-W. Lee, H.-D. Kim, Fabrication of transparent MgAl₂O₄ spinel through homogenous green compaction by microfluidization and slip casting, *Ceram. Int.* 41 (10) (2015) 13354–13360.
- [30] S.M. Olhero, I. Ganesh, P.M. Torres, J.M. Ferreira, Surface passivation of MgAl₂O₄ spinel powder by chemisorbing H₃PO₄ for easy aqueous processing, *Langmuir* 24 (17) (2008) 9525–9530.
- [31] P. Ramavath, P. Biswas, K. Rajeswari, M.B. Suresh, R. Johnson, G. Padmanabham, C.S. Kumbhar, T.K. Chongdar, N.M. Gokhale, Optical and mechanical properties of compaction and slip cast processed transparent polycrystalline spinel ceramics, *Ceram. Int.* 40 (4) (2014) 5575–5581.
- [32] C. Gajdoski, J. Böhmeler, Y. Lorgouilloux, S. Lemonnier, S. d’Astorg, E. Barraud, A. Leriche, Influence of post-HIP temperature on microstructural and optical properties of pure MgAl₂O₄ spinel: From opaque to transparent ceramics, *J. Eur. Ceram. Soc.* 37 (16) (2017) 5347–5351.
- [33] S. Guo, H. Wang, P. Xu, B. Wang, Y. Xiong, B. Tu, W. Wang, Z. Fu, Effect of pretreated microstructure on subsequent sintering performance of MgAl₂O₄ ceramics, *Ceram. Int.* 45 (6) (2019) 7544–7551.
- [34] K. Maca, M. Trunec, R. Chmelik, Processing and properties of fine-grained transparent MgAl₂O₄ ceramics, *Ceram. Silik.* 51 (2) (2007) 94.
- [35] A. Talimian, D. Galusek, Aqueous slip casting of translucent magnesium aluminate spinel: effects of dispersant concentration and solid loading, *Ceram. Int.* 45 (8) (2019) 10646–10653.
- [36] O. Schumacher, C.J. Marvel, M.N. Kelly, P.R. Cantwell, R.P. Vinci, J.M. Rickman, G.S. Rohrer, M.P. Harmer, Complexion time-temperature-transformation (TTT) diagrams: opportunities and challenges, *Curr. Opin. Solid State Mater. Sci.* 20 (5) (2016) 316–323.
- [37] A.R. Krause, A. Kundu, O. Kosasang, R.P. Vinci, M.P. Harmer, The influence of grain boundary area on the complexion time-temperature-transformation diagram of Eu-doped magnesium aluminate spinel, *Scr. Mater.* 178 (2020) 251–255.
- [38] A. Shafeiey, M.H. Enayati, A. Al-Haji, The effect of slip casting parameters on the green density of MgAl₂O₄ spinel, *Ceram. Int.* 43 (8) (2017) 6069–6074.
- [39] F. Mohammadi, O. Mirzaee, M. Tajally, The effects of ball milling time on the rheological, optical, and microstructural properties of YAG transparent ceramics, *Int. J. Appl. Ceram. Technol.* 17 (3) (2019) 1119–1127.
- [40] O. Schumacher, Thermodynamics and Kinetics of Complexion Transitions in Europium-doped MgAl₂O₄, Lehigh University, 2016, p. 123.
- [41] C.J. Marvel, A.R. Krause, M.P. Harmer, Effect of Eu-doping and grain boundary plane on complexion transitions in MgAl₂O₄, *J. Am. Ceram. Soc.* 104 (8) (2021) 4203–4213.

- [42] N. Nuns, F. Béclin, J. Crampon, Grain-boundary characterization in a nonstoichiometric fine-grained magnesium aluminate spinel: effects of defect segregation at the space-charge layers, *J. Am. Ceram. Soc.* 92 (4) (2009) 870–875.
- [43] N. Benameur, G. Bernard-Granger, A. Addad, S. Raffy, C. Guizard, Sintering analysis of a fine-grained alumina-magnesia spinel powder, *J. Am. Ceram. Soc.* 94 (5) (2011) 1388–1396.
- [44] P. Ghosh, R. Marder, A. Berner, W.D. Kaplan, The influence of temperature on the solubility limit of Ca in alumina, *J. Eur. Ceram. Soc.* 40 (15) (2020) 5767–5772.